




Magnetodielectric effect and spin state of iron ions in iron-substituted bismuth pyrostannate

Lubov Udod^{1,2,a} , Sergey Aplesnin^{1,2}, Maxim Sitnikov², Oxana Romanova¹, Oleg Bayukov¹, Alexander Vorotinov¹, Dmitriy Velikanov¹, Gennadiy Patrino^{1,3}

¹ Federal Research Center KSC SB RAS, Kirensky Institute of Physics, Akademgorodok 50, Krasnoyarsk, Russia 660036

² Siberian State University of Science and Technology, Krasnoyarsk, Russia 660037

³ Siberian Federal University, Krasnoyarsk, Russia 660041

Received: 1 April 2020 / Accepted: 16 September 2020

© Società Italiana di Fisica and Springer-Verlag GmbH Germany, part of Springer Nature 2020

Abstract The magnetic and magnetodielectric properties of bismuth pyrostannate $\text{Bi}_2(\text{Sn}_{1-x}\text{Fe}_x)_2\text{O}_7$ ($x = 0.1$ and 0.2) have been examined. Using the Mössbauer spectroscopy and electron paramagnetic resonance, the high-spin state and crystallographic positions of iron ions have been established. The coexistence of triclinic symmetry domains in the $\text{Bi}_2(\text{Sn}_{1-x}\text{Fe}_x)_2\text{O}_7$ ($x = 0.1$) compound with the monoclinic symmetry below 140 K has been found. For the $\text{Bi}_2(\text{Sn}_{1-x}\text{Fe}_x)_2\text{O}_7$ composition with $x = 0.2$, the nonlinear field dependence of magnetization in the paramagnetic region up to room temperatures has been observed. The electric polarization hysteresis and the magnetoelectric effect in the $\text{Bi}_2(\text{Sn}_{1-x}\text{Fe}_x)_2\text{O}_7$ compound have been disclosed. The magnetic field-dependent anomalous behavior of magnetization has been explained by the magnetoelectric effect.

1 Introduction

The compounds with a pyrochlore structure undergo the structural, magnetic, and ferroelectric phase transitions, which are usually accompanied by abrupt changes in the dielectric, mechanical, optical, and other properties [1]. Bismuth pyrostannate $\text{Bi}_2\text{Sn}_2\text{O}_7$ belongs to the family of pyrochlores, in which spin ice is implemented, similar to the $\text{Ho}_2\text{Ti}_2\text{O}_7$, $\text{Dy}_2\text{Ti}_2\text{O}_7$, and other compounds [2,3]. In these materials, magnetic ions are located at the vertices of a three-dimensional grid of regular tetrahedra. Due to the strong anisotropy, the magnetic moments can be directed either toward the center of each tetrahedron or in the reversed direction. The magnetic moments have three nearest neighbors with frustrated exchange couplings.

Bismuth pyrostannate is a dielectric. Substitution of iron for tin causes the magnetic ordering in the $\text{Bi}_2\text{Sn}_2\text{O}_7$ compound and, due to the interaction between the magnetic and ferroelectric subsystems, one can expect the manifestation of the magnetoelectric effect. Iron ions in the $\text{Bi}_2(\text{Sn}_{1-x}\text{Fe}_x)_2\text{O}_7$ compound can induce crystal structure distortions and a shift of the temperature of the phase transition. In particular, the heterovalent substitution of tin ions for 3d elements changes the temperature of the $\alpha \rightarrow \beta$ transition in $\text{Bi}_2\text{Sn}_2\text{O}_7$ [4–7]. The

^a e-mail: luba@iph.krasn.ru (corresponding author)

isovalent substitution of Bi^{3+} for Y^{3+} stabilizes the β phase at room temperature and normal pressure [8]. In iron oxides, the trivalent state of iron ions is most stable. Possibly, the isovalent substitution of Fe^{3+} for Bi^{3+} is energetically more favorable than the nonstoichiometric substitution for Sn^{4+} with the formation of vacancies in the anion subsystem.

Ferroelectrics with the magnetic field-induced polarization are second-type multiferroics [9], which are characterized by a strong magnetoelectric coupling caused by the antisymmetric exchange and a cycloid magnetic structure. The magnetic field-induced ferroelectric properties were observed in several spin-frustrated systems, including $\text{Ni}_3\text{V}_2\text{O}_8$ [10], $\text{Ba}_{0.5}\text{Sr}_{1.5}\text{Zn}_2\text{Fe}_{12}\text{O}_{22.6}$ [11], and MnWO_4 [12]. In all these materials, the ferroelectric behavior in the noncollinear magnetic phase was established, which can be explained in the framework of the spin current model.

In [13–16], the magnetic structure of delafossite CuFeO_2 (sp. gr. $R\bar{3}m$) with a two-dimensional triangular lattice was studied by neutron diffraction. The spontaneous polarization in a magnetic field of 7 T at the transition from the four-sublattice (CM-4) to noncollinear (NC) structure was observed [14]. Substitution of Fe for Ga induces the transition from the CM-4 to NC structure in zero magnetic field [15]. The noncollinear ordering of spins occurs under the long-range exchange interaction up to the 3rd coordination sphere ($J_1/k_B = -2.7$ K, $J_2/k_B = 3.0$ K, $J_3/k_B = 1.8$ K, $J_0/k_B = 0.93$ K, and $J_{00}/k_B = 1.9$ K) at a negative single-ion anisotropy constant of $D/k_B = -0.33$ K due to the strong spin–lattice interaction [15, 16]. The electric polarization attains a value of $200 \mu\text{C}/\text{m}^2$ at 4 K [16] and is explained using the spin current model [17]. In the $\text{Bi}_2(\text{Sn}_{1-x}\text{Fe}_x)_2\text{O}_7$ compound, the angle of the Fe–O–Fe exchange interaction is noticeably larger than that in delafossite (96°) [15]; therefore, one can expect an increase in the antiferromagnetic exchange by an order of magnitude and, correspondingly, the growth of the temperature of the transition to the magnetically ordered state.

Iron-substituted bismuth pyrostannate $\text{Bi}_2(\text{Sn}_{1-x}\text{Fe}_x)_2\text{O}_7$ ($x = 0.2$) undergoes a low-temperature shift-type transition at 140 K, which is related to the change in the Bi–O–Me bond length. This transition is accompanied by the lattice strain and manifests itself as a maximum in the temperature dependence of the thermal expansion coefficient [18]. Several low-temperature structural transitions were observed in the pyrochlore compounds, e.g., in $\text{Cd}_2\text{Nb}_2\text{O}_7$ [19]. In the temperature range from 10 to 300 K, this compound undergoes a sequence of five phase transitions; it is an improper ferroelectric below $T_S = 205$ K, a proper ferroelectric below $T_C = 196$ K, an incommensurate phase below $T_{\text{inc}} = 85$ K, a commensurate phase below $T_{\text{com}} = 46$ K, and a glass below $T_q = 18$ K. The changes in the domain structure and refractive index and the crystal symmetry lowering in the temperature range of 180–192 K are not observed. At temperatures below T_C , the ferroelectric domains coexist with domains of a preceding phase, which gradually decrease and become optically indistinguishable at 150 K. The temperatures of the ferroelectric transition correspond to the temperatures of the structural transition. In particular, the cubic structure $Fd\bar{3}m$ passes to the tetragonal one at $T_S = 205$ K and, as the temperature decreases to $T_{\text{inc}} = 85$ K, becomes monoclinic. At low temperatures, the displacement of Nb ions leads to the occurrence of short and long Nb–O bonds. In the intermediate phase, there are long and short bonds alternating along the [001] and [111] directions. The Nb1–O bond along the [100] direction is distorted during the transition to the monoclinic structure.

The octahedron distortion related to the change in the bond length, for example, the octahedron elongation, may lead to the change in the Fe^{3+} spin state. For the $3d^5$ configuration $t_{2g}^3 e_g^2$, according to the Tanabe–Sugano diagram [20], the high-spin ground state in the octahedral ligand field corresponds to the ground term ${}^6A_{1g}$ and the low-spin state with the

configuration t_{2g}^5 corresponds to the term ${}^2T_{2g}$. The change in the spin state is related to the transfer of two electrons from the e_g orbitals to the t_{2g} orbital.

In view of the aforesaid, the aim of this study is to establish the spin state, iron ion positions in the crystal structure, magnetic characteristics, electric polarization, and magnetoelectric interaction in bismuth pyrostannate $\text{Bi}_2(\text{Sn}_{1-x}\text{Fe}_x)_2\text{O}_7$ ($x = 0.1$ and 0.2).

2 Experimental

The $\text{Bi}_2(\text{Sn}_{1-x}\text{Fe}_x)_2\text{O}_7$ ($x = 0.1$ and 0.2) samples were obtained by the solid-state synthesis. They correspond to a Pc monoclinic cell in the α phase of $\text{Bi}_2\text{Sn}_2\text{O}_7$ [18].

The state and positions of iron ions were determined from the Mössbauer spectra measured at room temperature on an MS-1104Em spectrometer with a $\text{Co}^{57}(\text{Rh})$ source on powder absorbers with a thickness of 5–10 mg/cm^2 . The low iron concentration and high content of heavy bismuth atoms did not allow us to record high-quality spectra.

The electron spin resonance (ESR) study was carried out on a Bruker Elexsys E-580 spectrometer operating in the X band at temperatures of 110–300 K. The modulation frequency and amplitude were 100 kHz and 1 Oe, respectively. The temperature was stabilized by an Oxford ITC 503C temperature controller in an Oxford ESR 900 flow cryostat. In this cryostat, a resonator is kept at room temperature with a constant Q factor of ~ 9300 over the entire investigated temperature range.

The magnetic properties were studied on a MPMS-XL Magnetic Property Measurement System in magnetic fields of up to $H = 50,000$ Oe in the temperature range of 4–300 K.

The polarization was determined using the current measurements on a Keithley 6517B electrometer in electric fields at a frequency of $\nu = 0.01$ Hz on tableted samples with a diameter of 8 mm and height of 3 mm. Two measurement cycles were performed on the samples with two upper and one lower copper contacts. The magnetoelectric interaction was established from the induced electric polarization in magnetic fields of up to 13 kOe.

3 Results and discussion

3.1 Mössbauer study

Mössbauer spectra with a shape of asymmetric doublets are presented in Fig. 1a. Recording high-quality spectra was complicated by the low iron content and the presence of bismuth cations in the samples. Nevertheless, it makes sense to evaluate the valence state and arrangement of iron cations, which affect the magnetic properties of the investigated crystals.

The number of maxima in the P(QS) distribution points out the number of possible nonequivalent states or positions of iron. The P(QS) distributions for the $\text{Bi}_2(\text{Sn}_{1-x}\text{Fe}_x)_2\text{O}_7$ ($x = 0.2$) samples are shown in Fig. 1b. The P(QS) distribution in the sample with $x = 0.2$ has two maxima at different values of the isomer shift (IS) and the quadrupole splitting (QS), which correspond to two nonequivalent positions of iron ions.

At the next stage of the spectra decoding, using the data obtained from the P(QS) distributions, a model spectrum was built, which has two doublets at $x = 0.2$ and is fitted to the experimental spectrum. In this case, the hyperfine parameters were refined. The fitting results are given in Table 1.

The chemical shifts and quadrupole splittings of the iron positions in the investigated pyrostannates correspond to Fe^{3+} in the high-spin state in the octahedral oxygen coordination.

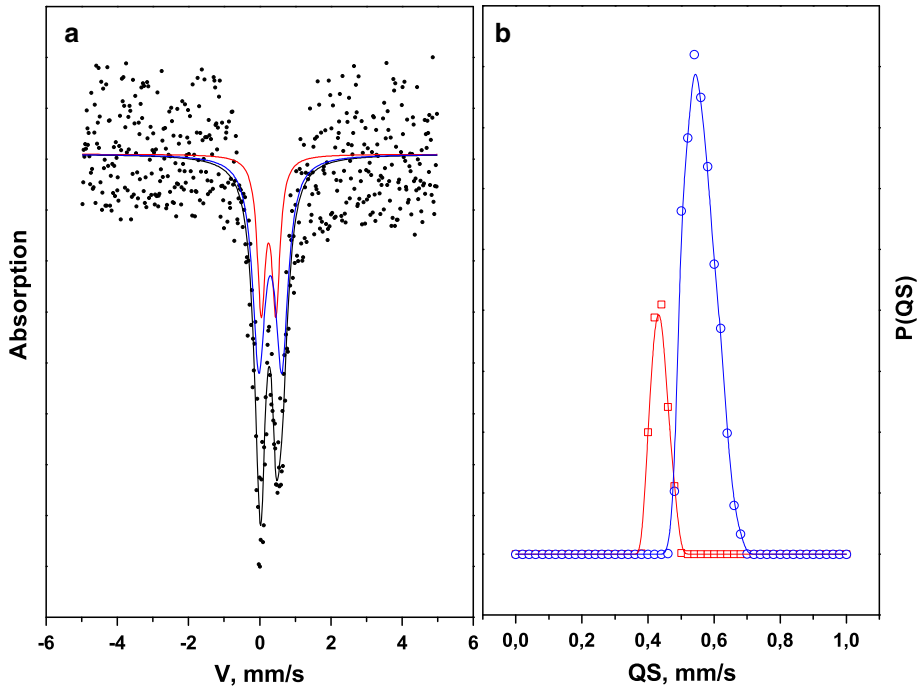


Fig. 1 **a** Mössbauer spectra of $\text{Bi}_2(\text{Sn}_{1-x}\text{Fe}_x)_2\text{O}_7$ ($x = 0.2$). **b** Probability of the quadrupole splitting distribution

Table 1 Mössbauer parameters of the $\text{Bi}_2(\text{Sn}_{1-x}\text{Fe}_x)_2\text{O}_7$ ($x = 0.2$) compound. IS is the isomer chemical shift relative to $\alpha\text{-Fe}$ [21], QS is the quadrupole splitting, W is the absorption line width, and A is the area under the partial doublet (position occupancy)

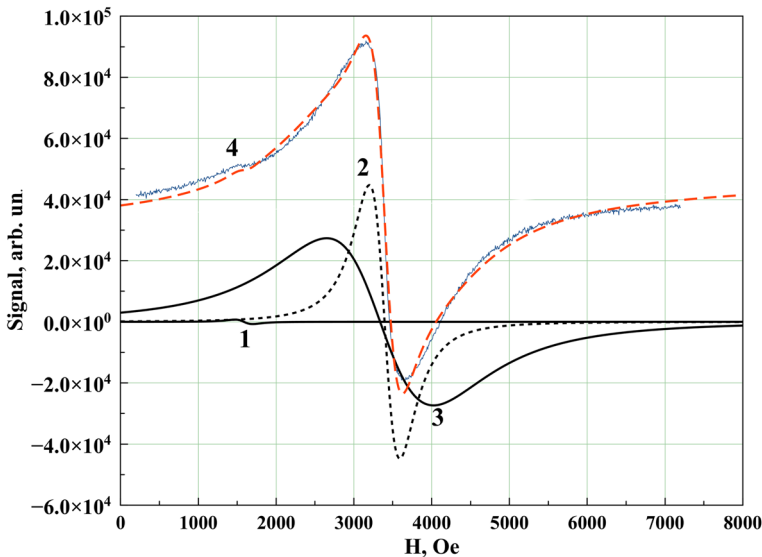
x	IS, mm/s ± 0.02	QS, mm/s ± 0.04	W, mm/s ± 0.04	A, % ± 0.05	Position of Fe
0.2	0.36	0.41	0.27	0.32	Fe1- Fe^{3+} (6)
	0.41	0.64	0.43	0.68	Fe2- Fe^{3+} (6)

In the first approximation, the isomer chemical shift is consistent with the charge electron density at the core of a Mössbauer atom. The shorter the interatomic spacing, the higher the electron density at the nucleus and the smaller the chemical shift. At the same time, the quadrupole splitting is directly proportional to the electric field gradient induced by the nearest local environment. For the Fe^{3+} cation, the charges of surrounding ions make a decisive contribution to the electric field gradient (EFG). Based on these correlations, we can estimate the probability of crystallographic position of iron cations.

According to the X-ray diffraction data [22], there are four crystallographically nonequivalent octahedra positions of tin in bismuth pyrostannate, which differ in the local symmetry. Table 2 gives the average interionic spacings Sn-O ($\langle r \rangle$) for the $\text{Bi}_2\text{Sn}_2\text{O}_7$ octahedra and the main components of the EFG induced by anions of the coordination octahedron. The relatively short interionic spacings and low calculated gradients for crystallographic positions Sn1 and Sn2 can be attributed to the small chemical shifts and quadrupole splittings of the Fe1 Mössbauer positions (Table 1). The relatively long interionic spacing and the high

Table 2 Sn-O interionic spacings and main component of the EFG induced by the oxygen octahedron in $\text{Bi}_2\text{Sn}_2\text{O}_7$ [22]

Sn position	$\langle r \rangle$, Å	EFG, $\text{e}/\text{Å}^3$
Sn1	2.052	0.032
Sn2	2.040	0.058
Sn3	2.075	0.110
Sn4	2.065	0.043

**Fig. 2** Typical magnetic resonance spectrum for $\text{Bi}_2(\text{Sn}_{1-x}\text{Fe}_x)_2\text{O}_7$ ($x = 0.2$). Lines 1, 2, and 3 are the Lorentzian fitting lines, and line 4 corresponds to the experimental spectrum. The dotted line shows the sum of the fitting curves

EFG of position Sn3 can correspond to the Fe2 Mössbauer position. The absence of explicit correlations for the Sn4 crystallographic position leaves the question about the population of this position with iron unanswered.

In fact, this conclusion should be considered rough, since the iron impurity cations can noticeably change the local lattice symmetry of the basic compound.

3.2 Electron spin resonance

The positions and spin state of iron ions and local deformations of the octahedron in the bismuth pyrostannate crystal lattice were studied electron spin resonance (ESR).

Figure 2 shows the spin resonance spectrum of the $\text{Bi}_2(\text{Sn}_{1-x}\text{Fe}_x)_2\text{O}_7$ ($x = 0.2$) compound at a temperature of 268 K. The experimental spectrum is described by three Lorentzian lines; the resulting curve (dashed line) corresponds to the experimental results. The weaker integral intensity of line 1 as compared with lines 2 and 3 is indicative of the low concentration of iron ions in the strongly distorted octahedral positions in both samples [23–25].

Line 1 (Fig. 2) in the spin resonance spectrum corresponds to the strongly distorted Fe^{3+} octahedral positions (the ratio between the parameters $D = 3/2D_z$ and $E = 1/2(D_x - D_y)$ is about $D/E \sim 3$ [23–25]).

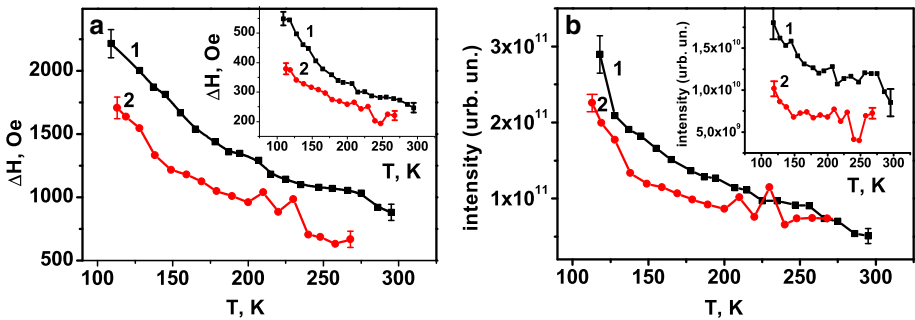


Fig. 3 Temperature dependences of (a) the width of line 2 in the ESR spectrum and (b) the integral intensity of $\text{Bi}_2(\text{Sn}_{1-x}\text{Fe}_x)_2\text{O}_7$. Line 1 corresponds to $x = 0.1$ and line 2, to $x = 0.2$. Insets: temperature dependences of the width of line 3 in the ESR spectrum at $x = 0.1$ and 0.2

The width ΔH (Fig. 3a) and intensity (Fig. 3b) of lines 2 and 3 for the $\text{Bi}_2(\text{Sn}_{1-x}\text{Fe}_x)_2\text{O}_7$ ($x = 0.1$ and 0.2) samples grow with a decrease in temperature. The difference between the widths of lines 2 and 3 is related to the degree of distortion of the octahedra. An increase in the width of these lines upon cooling is caused by an increase in the relaxation time with increase in density of crystallographic domain walls. An increase in the integral intensity of these lines upon cooling is indicative of the change in the population of the levels in a magnetic field and typical of the paramagnetic state of Fe^{3+} ions.

The temperature dependences of the ESR line width and intensity have anomalies in the region of the low-temperature phase transition ($T = 130$ K) and in the range of 210–250 K. With increase in concentration, these anomalies become more intense and correspond to the anomalies in the temperature dependence of the thermal expansion coefficient, as was shown in [18], where the shift-type structural transition in the $\text{Bi}_2(\text{Sn}_{1-x}\text{Fe}_x)_2\text{O}_7$ ($x = 0.2$) compound was observed. In the temperature range of 200–250 K, such a transition occurs under deformation of the SnO_6 octahedra. It is observed as the rotation and change of the octahedra slope angle, as well as the change in the metal–oxygen bond lengths. The symmetry remains unchanged. After that, at $T = 140$ K, all domains pass to the lower syngony and the sample becomes single phase.

The g factor was determined as a ratio between the measuring frequency ν ($\nu = 9.47$ and 9.44 GHz for $x = 0.1$ and 0.2 , respectively) and the resonance field H_{res} corresponding to the maximum absorption using the relation $h\nu = g\beta H_{\text{res}}$, where h is the Planck's constant and β is the Bohr magneton. The temperature dependence of the g factor for the $\text{Bi}_2(\text{Sn}_{1-x}\text{Fe}_x)_2\text{O}_7$ ($x = 0.1$ and 0.2) compounds (lines 2 and 3) is presented in Fig. 4.

As the temperature decreases, the g factor increases and changes most in the region of the monoclinic \rightarrow triclinic structural phase transition in $\text{Bi}_2(\text{Sn}_{1-x}\text{Fe}_x)_2\text{O}_7$ with two concentrations x at 140 K. The concentration phase transition has the prerequisites of a second-order transition. Lines 2 and 3 (Fig. 2) with a g factor of $g \sim 2$ in fields of about 3300 Oe correspond to the trivalent iron ions Fe^{3+} located in the octahedral sites in the s state. In the absence of spin-orbit coupling, the g factor of the orbital singlet is equal to the g factor of a free electron. Due to the spin-orbit coupling, the excited orbital states are admixed to the ground state and the orbital moment is unfrozen.

According to the Mössbauer and ESR data, iron ions are in the high-spin Fe^{3+} state and occupy octahedral sites. In the bismuth pyroostannate crystal lattice, the octahedral environment of Fe^{3+} ions is distorted, which leads to the splitting of the e_g and t_{2g} states. Upon

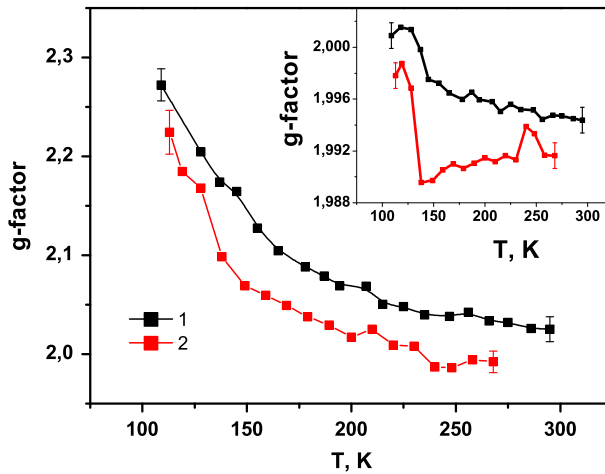


Fig. 4 Temperature dependence of the *g* factor of $\text{Bi}_2(\text{Sn}_{1-x}\text{Fe}_x)_2\text{O}_7$ with $x = (1)$ 0.1 and (2) 0.2 for line 2 of the ESR spectrum. Inset: temperature dependence of line 3 of the ESR spectrum

heterovalent substitution of Fe^{3+} ions for Sn^{4+} ones, the further distortion of local positions occurs through the formation of oxygen vacancies.

3.3 Magnetic properties

The temperature dependences of the magnetic susceptibility of the $\text{Bi}_2(\text{Sn}_{1-x}\text{Fe}_x)_2\text{O}_7$ ($x = 0.1$ and 0.2) compound measured in a magnetic field of 600 Oe are typical of paramagnets.

Figure 5 shows the reciprocal magnetic susceptibility of $\text{Bi}_2(\text{Sn}_{1-x}\text{Fe}_x)_2\text{O}_7$ ($x = 0.1$ and 0.2) as a function of temperature. For the composition with $x = 0.1$, the temperature dependence of $1/\chi$ is described by the Curie–Weiss law $1/\chi = (T - \Theta)/C$ with negative $\Theta = -10$ K over the entire temperature range. The effective magnetic moment of the Fe^{3+} ion on the crystal lattice site was calculated using the formula

$$\mu_{\text{eff}} = \sqrt{\frac{8C}{n}}, \tag{1}$$

where C is calculated from the temperature dependence of the inverse susceptibility and n is the number of iron ions in $\text{Bi}_2(\text{Sn}_{1-x}\text{Fe}_x)_2\text{O}_7$ ($x = 0.1$ and 0.2).

The effective magnetic moment of iron ions in the $\text{Bi}_2(\text{Sn}_{1-x}\text{Fe}_x)_2\text{O}_7$ ($x = 0.1$) compound determined using Eq. (1) is $\mu_{\text{eff}} = 5.76\mu_B$. The theoretical value of the magnetic moment of Fe^{3+} ions in the high-spin state with $S = 5/2$ and $g = 2$, according to the equation

$$\mu_S = g\sqrt{S(S + 1)}\mu_B, \tag{2}$$

is $\mu_S = 5.92\mu_B$. Based on the experimental data, we calculate the *g* factor using Eq. (2) and find it to be $g = 1.95$.

The temperature dependence of the inverse susceptibility of the $\text{Bi}_2(\text{Sn}_{1-x}\text{Fe}_x)_2\text{O}_7$ ($x = 0.2$) compound has an inflection point near the structural transition at 130–140 K, which is related to weakening of the antiferromagnetic interaction during the transition to the monoclinic crystal structure.

In the temperature range of 20–130 K, the paramagnetic Curie temperature is $\Theta_1 = -39.2$ K and, in the range of 130–230 K, it is $\Theta_2 = -9.2$ K. At the phase transition from

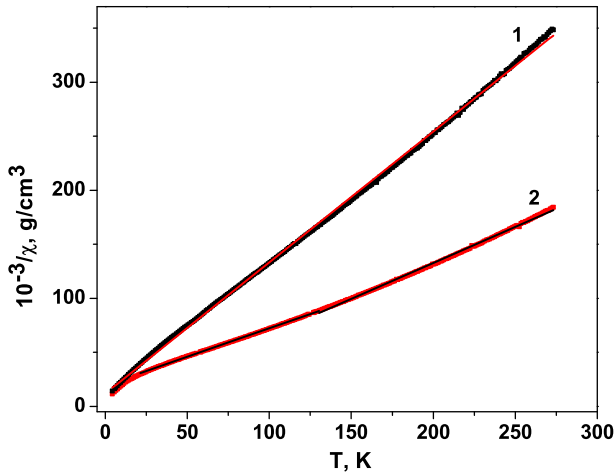


Fig. 5 Temperature dependence of the inverse magnetic susceptibility of $\text{Bi}_2(\text{Sn}_{1-x}\text{Fe}_x)_2\text{O}_7$ with $x = (1)$ 0.1 and (2) 0.2 in a magnetic field of 600 Oe

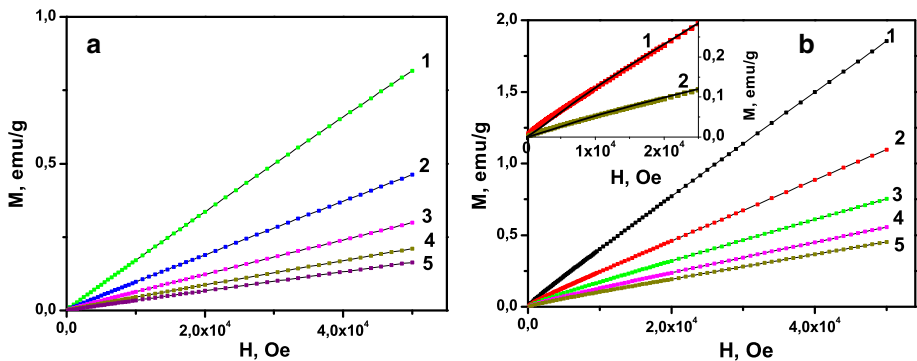


Fig. 6 Field dependence of magnetization of $\text{Bi}_2(\text{Sn}_{1-x}\text{Fe}_x)_2\text{O}_7$ with $x = (a)$ 0.1 and (b) 0.2 at different temperature: Curve 1 corresponds to 30 K; curve 2, to 60 K; curve 3, to 100 K; curve 4, to 150 K; and curve 5, to 200 K. Inset in **a**: 5 K; curve 1 for $x = 0.1$ and curve 2 for $x = 0.2$. Inset in **b**: $\text{Bi}_2(\text{Sn}_{1-x}\text{Fe}_x)_2\text{O}_7$ ($x = 0.2$)

the triclinic to monoclinic structure, the effective magnetic moment decreases from $\mu_{\text{eff}1} = 6.3\mu_B$ to $\mu_{\text{eff}2} = 5.77\mu_B$, which corresponds to the change in the g factor from $g_1 = 2.13$ to $g_2 = 1.95$. The change in the g factor with temperature is consistent with the ESR data. The obtained effective magnetic moment corresponds to the high-spin state of Fe^{3+} ions. In bismuth pyroostannate $\text{Bi}_2(\text{Sn}_{1-x}\text{Fe}_x)_2\text{O}_7$ ($x = 0.2$) with the triclinic symmetry, the antiferromagnetic interactions are four times stronger than the exchange in the monoclinic lattice and the sign of the relative g -factor variation with respect to the electron spin g factor ($\Delta g = g_{1,2} - 2$) changes.

The field dependences of the magnetization for the $\text{Bi}_2(\text{Sn}_{1-x}\text{Fe}_x)_2\text{O}_7$ compound with $x = 0.1$ and 0.2 are nonlinear (Fig. 6).

The magnetic measurements confirm the trivalent state of iron ions. The nonlinear behavior of the magnetization in magnetic fields of up to 50 kOe in the paramagnetic state at temperatures of up to 200 K is caused by the magnetoelectric effect (see below).

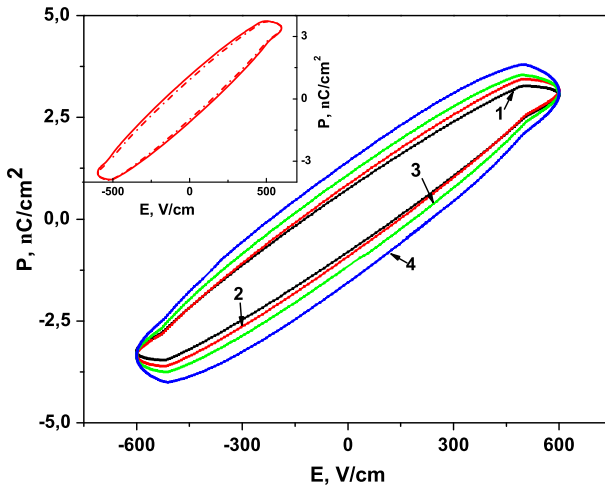


Fig. 7 Electric field dependence of polarization of $\text{Bi}_2(\text{Sn}_{1-x}\text{Fe}_x)_2\text{O}_7$ ($x = 0.2$) at different temperatures in a magnetic field of 12 kOe. Curve 1 corresponds to 120 K; curve 2, to 160 K; curve 3, to 200 K, and curve 4, to 280 K. Inset: 160 K; the dash-and-dot line corresponds to $H = 0$ and the solid line, to $H = 12$ kOe

3.4 Polarization

The electric polarization $P(E, H)$ induced by electric and magnetic fields was determined using the relation $P = \int j dt$ by measuring the current in an external quasi-periodic field with a frequency of $\nu = 0.01$ Hz. The measurements were performed at the two electric field polarities in magnetic fields of $H = 12$ kOe and $H = 0$. The room-temperature electrical resistance is $7.3 \cdot 10^{11}$ Ohm. Leakage currents are insignificant.

The $\text{Bi}_2(\text{Sn}_{1-x}\text{Fe}_x)_2\text{O}_7$ ($x = 0.1$) compound exhibits the paraelectric properties; the polarization is linear up to $T = 300$ K and obeys the law $P = \epsilon_0 \chi E$, where ϵ_0 is the dielectric constant, χ is the susceptibility, and E is the electric field. In the $\text{Bi}_2(\text{Sn}_{1-x}\text{Fe}_x)_2\text{O}_7$ ($x = 0.2$) compound, the symmetric $P(E)$ hysteresis loops were found. Figure 7 shows field dependences of the polarization obtained at different temperatures in a magnetic field of 12 kOe for the $\text{Bi}_2(\text{Sn}_{1-x}\text{Fe}_x)_2\text{O}_7$ ($x = 0.2$) compound. The inset in Fig. 7 shows the field dependence of polarization in magnetic fields of $H = 0$ and 12 kOe at $T = 160$ K.

Bismuth pyrostannate has a domain crystal structure [26] and, upon heterovalent substitution of bismuth for iron, vacancies are formed in the cationic and anionic sublattices, which leads to the formation of the donor and acceptor impurity states. Delocalized electrons from the impurity states diffuse and are accumulated in traps on intercrystalline domain walls. Under the action of an external electric field, carriers diffuse to the domain surface and are localized in traps. As a result, the intercrystalline boundaries are charged, which broadens the hysteresis loop. There exist several models that explain the hysteresis loop broadening. The most common of these models for bulk systems (crystals) are domain pinning on space charges accumulated on domain walls, pinning on the formed defect clusters, and formation of dipole defects, which affect the polarization [27–29]. The formation of charged walls and partial screening lead to the nonuniform potential distribution over the sample volume. The crystal structure rearrangement leads to the change in the defect density [30] and induces a space charge in the sample.

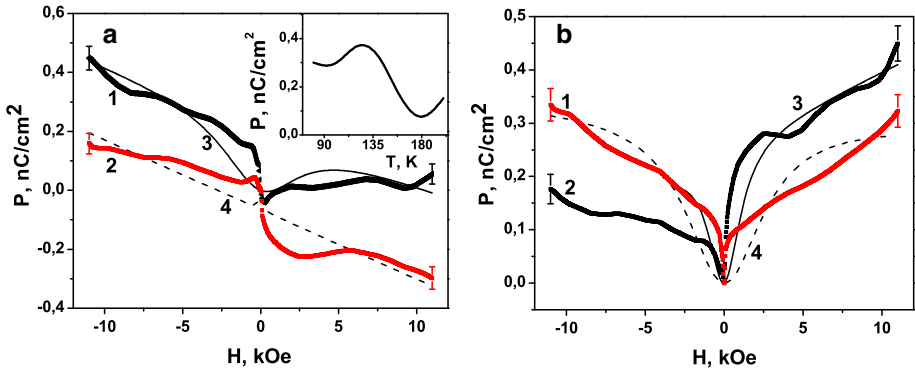


Fig. 8 Polarization of $\text{Bi}_2(\text{Sn}_{1-x}\text{Fe}_x)_2\text{O}_7$ ($x = 0.2$) vs. magnetic field at temperatures of **a** $T =$ (1) 120 and (2) 160 K. Theoretical calculations cared out by formula (4) with $d = 0.151/\text{kOe}^2$, $T = 120\text{ K}$ (3) with $A = -2.0 \cdot 10^{10}$, $B = 3.3 \cdot 10^{10}$, $T = 160\text{ K}$ (4) with $A = -2.2 \cdot 10^{10}$, $B = 1.3 \cdot 10^{10}$, **b** $T = 200\text{ K}$ (1), 280 K (2). Theoretical calculations cared out by formula (4) $T = 200\text{ K}$ (3) with $A = -1.2 \cdot 10^{10}$, $B = 4.3 \cdot 10^{10}$, $T = 280\text{ K}$ (4) with $A = -2 \cdot 10^{11}$, $B = 5 \cdot 10^{10}$. Inset: temperatures dependence of magnetic field-induced electric polarization

Upon heterovalent substitution, the most probable mechanism of the electron polarization is the occurrence of anion vacancies. Oxygen vacancies represent equivalent positive charges, near which, for compensation, impurity electrons are localized according to the electron neutrality principle.

3.5 Magnetolectric effect

We establish the magnetolectric interaction from the induced electric polarization in a magnetic field. Figure 8 shows the $P(H)$ dependence for the $\text{Bi}_2(\text{Sn}_{1-x}\text{Fe}_x)_2\text{O}_7$ ($x = 0.2$) compound in the temperature range of 80–300 K. A monotonic magnetic-field dependence of the polarization was found at all temperatures. The magnetolectric interaction is caused by the spin-orbit coupling with a linear field dependence and the electron–lattice interaction with a quadratic field dependence; therefore, we present the induced polarization in the form $P_i(H) = \alpha_{ij}H_j + \gamma_{ij}H_j^2$.

In the temperature range of 80–300 K, the components of the magnetolectric interaction tensor change their sign upon heating. At low temperatures (down to 120 K), the induced polarization is an even function of the magnetic field. In the region of the structural transition (140–160 K), the polarization changes its sign at the magnetic field inversion (Fig. 8a), which points out the existence of the linear magnetolectric effect. Further heating of the sample to room temperature leads to the predominance of the quadratic magnetolectric effect (Fig. 8b). The magnetic-field-induced electric polarization decreases upon heating (inset in Fig. 8a). The initial $\text{Bi}_2\text{Sn}_2\text{O}_7$ compound does not have an inversion center [31], which predetermines the magnetolectric effect [32].

A linear magnetolectric response exists in the materials with the magnetic and ferroelectric ordering, e.g., in multiferroics, where the parity and time-reversal symmetries are broken. In paramagnets, a linear response should be absent for the symmetry reasons. However, in a number of paramagnetic compounds, this effect is observed. A molecular magnetolectric consisting of two chiral isomers of ytterbium ions at room temperature is simultaneously a ferroelectric and a paramagnet [33]. This material exhibits magnetostriction, which determines the correlation between the magnetic and electrical properties: the reaction of ytterbium ions

to an external magnetic field induces the strain, which, in turn, changes the configuration of electric dipoles and, consequently, polarization [33]. The linear longitudinal magnetoelectric effect found in the α -Bi₂O₃ single crystal was attributed to the paramagnetic centers [34]. Perhaps, this effect is caused by valleys in the electron excitation spectrum of bismuth oxides. A new form of the linear magnetoelectric effect based on the degree of freedom of the valleys in a two-dimensional (2D) Dirac material was reported in [35]. These results agree well with the theoretical model of the valley magnetoelectricity driven by the Berry curvature effects [35].

The magnetoelectric effect is caused by electrons, which carry a charge and a magnetic moment (spin and orbital). Their interaction (exchange, spin-orbit, and Coulomb) correlates the motion of charges in space and the mutual arrangement of magnetic moments. The magnetoelectric effect can be caused by the orbital motion of electrons, since the orbital motion is related to the vector potential. The orbital magnetoelectric polarizability was studied in non-magnetic topological insulators [36]. These insulators have the Bloch wave functions with extraordinary topological properties, which lead to the magnetoelectric response described by the term $\mathbf{E} \cdot \mathbf{B}$ [36]. The orbital contribution of electrons to the frozen-lattice polarization induced by a magnetic field in band insulators was solved in [37,38]. The components of the magnetoelectric tensor change their sign depending on the phase of an electron [38].

The electric polarization induced by lattice straining in a magnetic field (magnetostriction) is fitted by the function

$$P = aH + b \frac{H^2}{1 + dH^2}, \quad (3)$$

where a , b , and d are the fitting parameters. Function (3) satisfactorily describes the experimental $P(H)$ data. The linear component dominates in the region of the structural phase transition to the triclinic syngony [18] at 140–160 K (Fig. 8a). The magnetoelectric effect is caused mainly by domain walls, impurity states, and structural inhomogeneities (heterostructures). The linear term in Eq. (3) is not associated with the fundamental symmetry requirements (the space parity and time-reversal symmetries). In the transition region, domain walls are formed between different phases with the strong spin-orbit coupling at the interface and the dominant orbital contribution to the magnetoelectric effect. In the bulk of the sample, the number of domain walls decreases with increase in temperature and, therefore, the quadratic magnetoelectric effect prevails.

The magnetization of the Bi₂(Sn_{1-x}Fe_x)₂O₇ ($x = 0.2$) solid solution can be presented as a function of the magnetic field in the paramagnetic region with three fitting parameters

$$M = \chi H + \alpha P = AH + B \frac{H^2}{1 + dH^2}. \quad (4)$$

The nonlinear $M(H)$ dependence (Fig. 6) is satisfactorily described by Eq. (4).

4 Conclusions

According to the Mössbauer and ESR spectra, iron ions in the pyrochlore crystal structure occupy two nonequivalent octahedral positions and are in the high-spin state. The antiferromagnetic exchange exists between the spins of iron ions, and the paramagnetic Curie temperature sharply increases with increase in concentration of iron ions. In the compound with $x = 0.2$, a decrease in the magnetic moment and weakening of the antiferromagnetic

exchange in the region of the structural phase transition from the triclinic to monoclinic structure were found.

In bismuth pyrostannate with $x = 0.2$, the nonlinear behavior of the magnetization in magnetic fields of up to 50kOe in the paramagnetic state at temperatures up to 200K was found and attributed to the magnetoelectric interaction. The magnetic-field-induced electric polarization is an even function of the field, except for the region of the structural phase transition, where the linear magnetoelectric effect dominates.

In the $\text{Bi}_2(\text{Sn}_{1-x}\text{Fe}_x)_2\text{O}_7$ ($x = 0.1$) compound, the electric polarization is a linear function of the electric field. With an increase in the iron ion concentration (at $x = 0.2$), the electric polarization hysteresis was detected in bismuth pyrostannate.

Acknowledgements This study was supported in part by the Russian Foundation for Basic Research, the Government of the Krasnoyarsk krai, and the Krasnoyarsk Territorial Foundation for Support of Scientific and R&D Activities, Project No. 18-42-240001 r_a «Inversion of the Sign of the Magnetoelectric Tensor Components on Temperature in Neodymium-Substituted Bismuth Ferrite Garnet Films» and by the Russian Foundation for Basic Research, Project No. 20-52-00005 bel_a.

References

1. F. Jonah, J. Sheerane, *Ferroelectric Crystals* (Mir, Moscow, 1981)
2. O.A. Petrenko, M.R. Lees, G. Balakrishnan, *Phys. Rev. B* **68**, 012406 (2003). <https://doi.org/10.1103/PhysRevB.68.012406>
3. L.R. Yaraskavitch et al., *Phys. Rev. B* **85**, 020410(R) (2012). <https://doi.org/10.1103/PhysRevB.85.020410>
4. S.S. Aplesnin, L.V. Udod, M.N. Sitnikov, *Ceram. Int.* **44**, 1614 (2018). <https://doi.org/10.1016/j.ceramint.2017.10.082>
5. S.S. Aplesnin, L.V. Udod et al., *Mater. Res. Express* **5**, 115202 (2018). <https://doi.org/10.1088/2053-1591/aaddd9>
6. S.S. Aplesnin, L.V. Udod et al., *IOP Conf. Ser.: Mater.Sci. Eng.* **467**(5), 012014 (2019). <https://doi.org/10.1088/1757-899X/467/1/012014>
7. S.S. Aplesnin, L.V. Udod et al., *Phys. Sol. St.* **59**, 2268 (2017). <https://doi.org/10.1134/S10663783417110038>
8. B.J. Ismunandar, Kennedy et al., *J. Solid State Chem.* **131**, 317 (1997)
9. D. Khomskii, *Physics* **2**, (2009). <https://doi.org/10.1103/Physics.2.20>
10. G. Lawes et al., *Phys. Rev. Lett.* **95**, 087205 (2005). <https://doi.org/10.1103/PhysRevLett.95.087205>
11. T. Kimura et al., *Phys. Rev. Lett.* **94**, 137201 (2005). <https://doi.org/10.1103/PhysRevLett.94.137201>
12. K. Taniguchi et al., *Phys. Rev. Lett.* **97**, 097203 (2006). <https://doi.org/10.1103/PhysRevLett.97.097203>
13. Sh Ishiwata et al., *Phys. Rev. B* **81**, 100411(R) (2010). <https://doi.org/10.1103/PhysRevB.81.100411>
14. N. Terada et al., *Phys. Rev. B* **73**, 014419 (2006). <https://doi.org/10.1103/PhysRevB.73.014419>
15. T. Fujita et al., *J. Phys. Soc. Jpn.* **82**, 064712 (2013). <https://doi.org/10.7566/JPSJ.82.064712>
16. T. Kimura et al., *Phys. Rev. B* **73**, 220401(R) (2006). <https://doi.org/10.1103/PhysRevB.73.220401>
17. T.A. Kaplan et al., *Phys. Rev. B* **83**, 174432 (2011). <https://doi.org/10.1103/PhysRevB.83.174432>
18. L.V. Udod, S.S. Aplesnin et al., *J. Alloys Compd.* **804**, 281 (2019). <https://doi.org/10.1016/j.jallcom.2019.07.020>
19. M. Fischer et al., *Phys. Rev.* **78**, 014108 (2008). <https://doi.org/10.1103/PhysRevB.78.014108>
20. Y. Wu et al., *JGR Solid Earth* **122**, 5935 (2017). <https://doi.org/10.1002/2017JB014095>
21. P. Gütllich, *Mössbauer Spectroscopy and Transition Metal Chemistry. Fundamentals and Applications* (Springer, Berlin, Heidelberg, 1978)
22. J.W. Lewis et al., *J. Am. Chem. Soc.* **138**, 8031 (2016). <https://doi.org/10.1021/jacs.6b04947>
23. G. Mathies et al., *J. Phys. Chem. B* **116**, 7122 (2012). <https://doi.org/10.1021/jp3025655>
24. G. Rama Sundari et al., *J. Non-Cryst. Solids* **365**, 6 (2013). <https://doi.org/10.1016/j.jnoncrysol.2013.01.023>
25. V. Vercamer et al., *J. Non-Cryst. Solids* **428**, 138 (2015). <https://doi.org/10.1016/j.jnoncrysol.2015.08.010>
26. R.D. Shannon et al., *J. Phys. Chem. Solids* **41**, 117 (1980)
27. M. Fischer et al., *Phys. Rev. B* **78**, 014108 (2008). <https://doi.org/10.1103/PhysRevB.78.014108>

28. M. Maczka et al., *Phys. Rev. B* **79**, 214437 (2009). <https://doi.org/10.1103/PhysRevB.79.214437>
29. S.S. Aplesnin, L.V. Udod et al., *Ceram. Int.* **42**, 5177 (2016). <https://doi.org/10.1016/j.ceramint.2015.12.040>
30. M. Kobune et al., *Jpn. J. Appl. Phys.* **37**, 5154 (1998)
31. I.R. Evans et al., *J. Mater. Chem.* **13**, 2098 (2003). <https://doi.org/10.1039/b305211g>
32. A.K. Zvezdin et al., *UFN* **179**, 887 (2009)
33. Jérôme Long et al., *Science* **367**, 671 (2020). <https://doi.org/10.1126/science.aaz2795>
34. V.I. Nizhankovskii et al., *Ferroelectrics* **279**, 157 (2002). <https://doi.org/10.1080/713716529>
35. J. Lee et al., *Nat. Mater.* **16**, 887 (2017). <https://doi.org/10.1038/nmat4931>
36. X.L. Qi et al., *Phys. Rev. B* **78**, 195424 (2008). <https://doi.org/10.1103/PhysRevB.78.195424>
37. M.A. Essin et al., *Phys. Rev. B* **81**, 205104 (2010). <https://doi.org/10.1103/PhysRevB.81.205104>
38. Andrei Malashevich et al., *New J. Phys.* **12**, 053032 (2010). <https://doi.org/10.1088/1367-2630/12/5/053032>